Proceedings of the ASME 2021
Verification and Validation Symposium
VVS2021
May 19-20, 2020, Virtual, Online

VVS2021-65231

RESPONSE EFFECTS DUE TO POLYGONAL REPRESENTATION OF PORES IN POROUS MEDIA THERMAL MODELS

Kevin W. Irick

Sandia National Laboratories[1]
P.O. Box 5800
Albuquerque, NM 87185-0828

and

Nima Fathi

The University of New Mexico
Albuquerque, NM, USA

ABSTRACT

Physics models—such as thermal, structural, and fluid models—of engineering systems often incorporate a geometric aspect such that the model resembles the shape of the true system that it represents. However, the physical domain of the model is only a geometric representation of the true system, where geometric features are often simplified for convenience in model construction and to avoid added computational expense to running simulations. The process of simplifying or neglecting different aspects of the system geometry is sometimes referred to as "defeaturing." Typically, modelers will choose to remove small features from the system model, such as fillets, holes, and fasteners. This simplification process can introduce inherent error into the computational model. A similar event can even take place when a computational mesh is generated, where smooth, curved features are represented by jagged, sharp geometries. The geometric representation and feature fidelity in a model can play a significant role in a corresponding simulation's computational solution. In this paper, a porous material system—represented by a single porous unit cell—is considered. The system of interest is a two-dimensional square cell with a centered circular pore, ranging in porosity from 1% to 78%. However, the circular pore was represented geometrically by a series of regular polygons with number of sides ranging from 3 to 100. The system response quantity under investigation was the dimensionless effective thermal conductivity, k^*, of the porous unit cell. The results show significant change in the resulting k^* value depending on the number of polygon sides used to represent the circular pore. In order to mitigate the convolution of discretization error with this type of model form error, a series of five systematically refined meshes was used for each pore representation. Using the finite element method (FEM), the heat equation was solved numerically across the porous unit cell domain. Code verification was performed using the Method of Manufactured Solutions (MMS) to assess the order of accuracy of the implemented FEM. Likewise, solution verification was performed to estimate the numerical uncertainty due to discretization in the problem of interest. Specifically, a modern grid convergence index (GCI) approach was employed to estimate the numerical uncertainty on the systematically refined meshes. The results of the analyses presented in this paper illustrate the importance of understanding the effects of geometric representation in engineering models and can help to predict some model form error introduced by the model geometry.

NOMENCLATURE

[1] This paper describes objective technical results and analysis. Any subjective views or opinions that might be expressed in the paper do not necessarily represent the views of the U.S. Department of Energy or the United States Government. *SAND2021-#### C*.

A = area
α = porosity
ε = error
Γ = domain boundary
h = characteristic mesh size
H = mesh number
k = thermal conductivity
$\boldsymbol{K}$ = thermal conductivity matrix
L = cell length
N = total quantity
$\boldsymbol{N}$ = shape function
Ω = domain
p = order of accuracy
q = heat flow
r = mesh refinement factor
R = radius
S = energy source
t = triangle index
T = temperature
$\boldsymbol{T}$ = triangle node temperature vector
U = uncertainty
W = cell width
x = x-coordinate
y = y-coordinate

Subscripts
α = pore
C = cold
eff = effective
f = formal
Γ = boundary
H = mesh number, hot
$Linf$ = L-infinity norm
MMS = manufactured solution
n = normal
num = numerical
RMS = root mean square
$sides$ = polygon sides
t = triangle
v = nodes

Superscripts
$*$ = dimensionless
$'$ = per unit length
$''$ = per unit area

1. INTRODUCTION

A porous material as a special case of heterogeneous materials includes voids (i.e., locales of material absence) within the bulk material. Effective properties are a means of describing the general behavior of the system—based on the characterization of the pertinent heterogeneities or conditions in the system. As engineering systems become increasingly complex, it can be advantageous—and even necessary—to use effective properties to analyze and predict system performance in a feasible manner. Such approaches can be useful in a variety of applications. It has been shown, for example, that the heterogeneous microstructures of thermal barrier coatings (TBCs) on gas power turbine blades at a material level have significant effects on the effective thermal conductivity of the TBCs. Effective thermal conductivity plays a significant role in the performance and longevity of the TBCs and consequently the turbine blades that they protect [1-5]. Furthermore, additive manufacturing technology—a form of which is commonly known as 3D printing--has made it possible to have computerized fabrication of porous structures in various forms including foam and lattice at different scales. This manufacturing process has a natural need for understanding thermal transport in porous materials—considering the non-homogenous and high-temperature processes used—where additive manufacturing can be used specifically for thermal applications [6-8]. The thermal performance and advantage of other advanced materials—such as aerogels and doped polymers—are driven by their heterogeneous characteristics and can be seen in marine, oil and gas, aerospace, energy, and thermal management industries [9-12]. The expansive set of industries and specific thermal applications where heterogeneous materials are of immediate consequence is immeasurable. Thus, the pursuit of measuring, analyzing, and predicting the thermal performance of such materials is in high demand.

While the effective thermal response of porous structures has attracted the attention of researchers recently, the configuration of pore structures--especially with the presence of sharp edges--have not been investigated thoroughly yet. The smaller pore size in various geometries is an inevitable topic in the future horizon of 3D printing technology and hierarchy porous structures. The main objective of the investigation covered in this paper is to study the effect of the existence of sharp edges in organized polygonal pore formats on the thermal behavior of a porous structure. In this work, high fidelity computational analyses are conducted and verified to obtain the effective thermal response of various pore polygonal geometries and study the variation of the thermal response with respect to the geometry of sharp edges for the same porosity value.

2. SYSTEM DESCRIPTION

In order to investigate possible implications of geometric fidelity and representation on porous material thermal responses, a porous unit cell system was defined in two dimensions to capture a fundamental porous material description. As shown in Figure 1, the two-dimensional unit cell has dimensions W and L in the $\boldsymbol{x}$ and $\boldsymbol{y}$ rectangular directions, respectively. The porous material is defined with a centered circular pore of radius, R_α, where, for the sake of this study, the negative and positive x boundaries and the pore wall boundary are made to be adiabatic. A temperature gradient is enforced across the domain, where the negative and positive y boundaries are held at hot and cold temperatures T_H and T_C, respectively. The prescribed temperature differential induces an average heat flow per unit length, q', across the hot and cold boundaries.

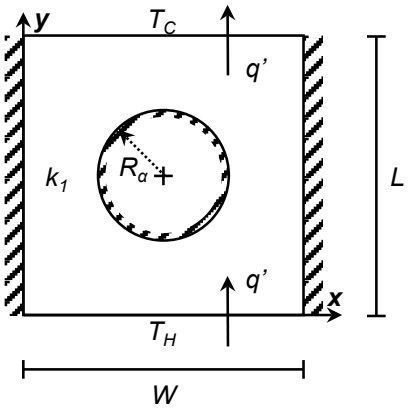

Figure 1. System of interest is two-dimensional unit cell with centered circular pore and enforced temperature gradient

The overall effective thermal conductivity of the porous system—in the direction of the system temperature gradient—is computed as

$$k_{eff} = \frac{q'L}{(T_H - T_C)W}. \quad (1)$$

The effective response is further non-dimensionalized as

$$k^* = k_{eff}/k_1, \quad (2)$$

where a k^* value less than 1 indicates a reduction in thermal conduction, and a value greater than 1 would indicate an increase in thermal conduction, with respect to the bulk material thermal conductivity. For this system, the characteristic geometry of the system of interest is porosity, α, which is the fraction of the unit cell occupied by the pore. Thus,

$$\alpha = \frac{\pi R_\alpha^2}{LW}. \quad (3)$$

A series of α values was considered for this study in the range of [1%,78%], where k^* changes as response to changing α. Previous work has spent a great deal of effort investigating this same system with respect to the k^*-α correlation [13-17]. However, this work is dedicated more specifically to understanding the impact of geometric representation of the circular pore on k^*. Although the true system of interest is the circular pore system shown in Figure 1, computational methods and model simplifications would often represent the smooth, continuous circular pore feature with some non-smooth, discontinuous representation, such as a polygon. Thus, for this study, each porous system—a single given circular pore size—is represented by a series of regular polygons with number of sides, N_{sides}, ranging from 3 to 100. Figure 2 illustrates the representation of a single circular porous system by regular polygons with 3, 4, and 5 sides, where the polygonal pore geometry is circumscribed by circular geometry which the polygonal geometry represents.

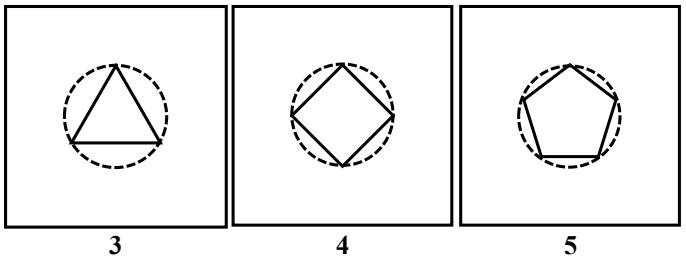

Figure 2. Multiple fixed polygonal representations used to represent the same circular pore

By controlling the geometric representation of the circular pores, the effects of geometric pore representation can be distinctly separated from the effects of porosity, where the former has model form error implications. The following section describes the computation methods used for these analyses that allow for the segregation of the model form and porosity dependence effects on the effective thermal response of the porous system.

3. SOLUTION APPROACH

To determine q', and, subsequently, k^*, in the system of interest the temperature distribution across the computational domain must be determined and is done so by solving the governing two-dimensional, steady state, isotropic heat transport equation,

$$k\left(\frac{\partial^2 T}{\partial x^2} + \frac{\partial^2 T}{\partial y^2}\right) + S = 0, \quad (4)$$

where k is thermal conductivity, T is temperature, x and y are rectangular positions, and S is the general heat source distribution.

The finite element (FE) method was used in this work to computationally solve the governing partial differential equation (PDE) of Equation (3) across the system. The FE method requires the discretization of both the domain and the governing PDE. Figure 3 illustrates the domain discretization into an unstructured triangular mesh, where each small triangle is a single finite element.

When using the FE method, the governing equation must be solved across each triangular element simultaneously. Discretization of the problem induces numerical error into the computational solution, U_{num}, where, for this study, U_{num} is computed for the ultimate system response quantity (SRQ) of k^*. As the mesh is refined (i.e., elements' sizes made smaller), the solution to the PDE and SRQ's derived from the solution are expected to change (even if slightly) and should begin to converge to single solution. The following subsections describe

the discretization of both the computational domain and the governing PDE.

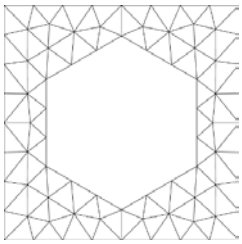

Figure 3. Discretization of computational domain into unstructured triangular elements

3.1 DOMAIN DISCRETIZATION

As described previously, prior to mesh generation, the polygonal geometric representation of the circular pore was fixed. Generally speaking, in most modeling workflows, the base geometry of a feature (in this case the circular pore) is defined such that the meshing algorithm creates elements across the domain, resulting in some geometric representation of the smooth, curved surfaces based on the sizes of the elements. In this system of interest, for example, the circular pore geometry would be assigned, some control mesh size would be prescribed, then the meshing algorithm would generate a mesh, resulting in a polygonal (not necessarily a regular polygon) model pore structure with N_{sides} being inherently dependent on the chosen mesh size and algorithm. However, in this study, the pore geometry assigned to the meshing algorithm was intentionally defined as a regular polygon so that N_{sides} would not be dependent on the mesh size or meshing algorithm.

Figure 4 illustrates a notional triangle element used in the FE discretization of the computational domain for this study. Each element is comprised of three nodes or vertices, where node i of triangle t is at location $(x_{t,i},y_{t,i})$ and has temperature $T_{t,i}$. The triangle itself occupies area A_t. For this study, three-node linear triangle elements were used for the FE method.

In order to facilitate methods for establishing code accuracy and estimating numerical uncertainty due to discretization, systematic mesh refinement was used to generate five, successively refined meshes for each given system (each α-N_{sides} combination). In each system mesh series, the five meshes are assigned a mesh number, H, from 5 to 1, where $H=5$ is the coarsest mesh and $H=1$ is the finest mesh in the series, respectively. For each mesh, a characteristic mesh size (or length), h_H, was computed as

$$h_H = \sqrt{\frac{1}{N_{t,H}} \Sigma_{t=1}^{N_{t,H}} A_t} \tag{5}$$

to describe the size of each mesh quantitatively. Here, $N_{t,H}$ is the total number of triangle elements in the mesh. Figure 5 shows an example of systematic mesh refinement for a single porous system model, where Figure 5a through Figure 5e show mesh $H=5$ through $H=1$, respectively. The meshes were refined systematically such that the mesh refinement factor, $r_{i,j}$, computed by Equation (6), from mesh $H=j$ to mesh $H=i$, was approximately 2.0, where j and i are the mesh numbers of the coarser and finer of two successive meshes in the refinement series, respectively.

$$r_{i,j} = h_j / h_i \tag{6}$$

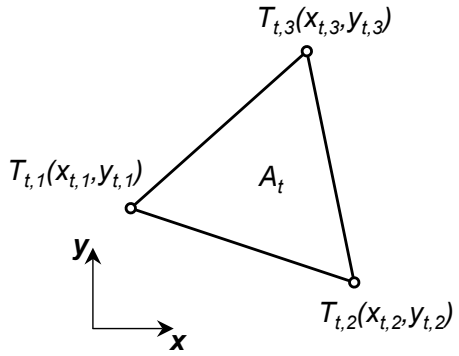

Figure 4. Notional linear triangle element

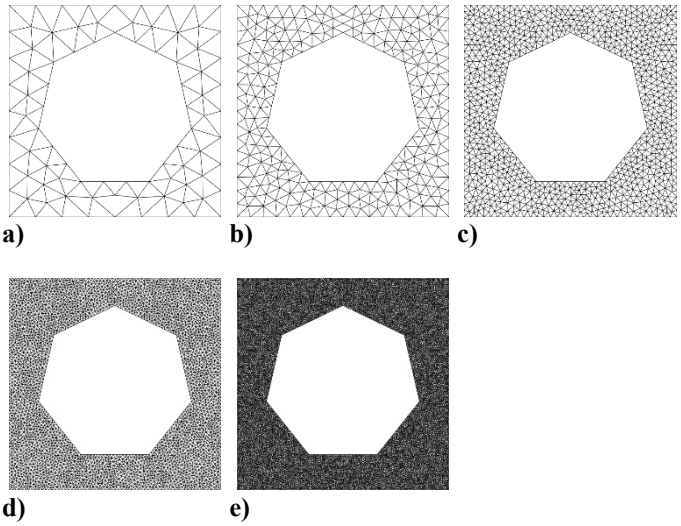

Figure 5. Example of systematic mesh refinement of a single computational domain

3.2 PDE DISCRETIZATION

The Galerkin FE method was employed as the computational approach to solving the governing heat equation across the discretized porous unit cell domain. The discretized form of Equation (4) can be expressed as

$$\int_{\Omega} (\boldsymbol{\nabla N})^T \boldsymbol{K} \boldsymbol{\nabla N} d\Omega \boldsymbol{T} = \int_{\Omega} \boldsymbol{N}^T S d\Omega - \int_{\Gamma} \boldsymbol{N}^T q_n'' d\Gamma, \quad (7)$$

which is solved for each linear triangle element simultaneously. In the discretized PDE, $\boldsymbol{N}$ is the linear interpolation shape function row vector for elemental field variables, $\boldsymbol{K}$ is the 2x2 thermal conductivity matrix, Ω is the element area, $\boldsymbol{T}$ is the three-element column vector of the temperatures at the triangle element nodes, q_n'' is the boundary normal heat flux on a triangle boundary, and Γ is the triangle boundary. In condensed matrix form Equation (7) looks like

$$\boldsymbol{GT} = \boldsymbol{P}, \quad (8)$$

where $\boldsymbol{G}$ is the conductance matrix and $\boldsymbol{P}$, is the three-row column vector for net heat load corresponding to the nodes with temperatures found in $\boldsymbol{T}$. The discretized PDE is solved iteratively using computational tools. The following section describes the computational evaluation of the discretized heat transfer problem and the associated methods.

4. COMPUTATIONAL EVALUATION

Geometric discretization (or mesh generation) of the computational domain was performed using the Gmsh software tool [18]. Personal FE element code [19] was used to solve Equation (8) across the computational domain, where a conjugate gradient solution update was used to drive down residuals in the energy balance. Equation (9) describes the element-wise three-row column vector for residual heat, $\boldsymbol{\rho}$, whose elements, ρ_i, express imbalance in the energy equation for each node.

$$\boldsymbol{\rho} = \boldsymbol{P} - \boldsymbol{GT} \quad (9)$$

The solution to the discretized PDE was updated on a given mesh H until the root mean square (RMS) of the mesh residuals, $\rho_{RMS,H}$, fell below $1.0\text{x}10^{-8}$, where

$$\rho_{RMS,H} = \sqrt{\frac{1}{N_{v,H}} \sum_{i=1}^{N_{v,H}} \rho_i^2}. \quad (10)$$

The L-infinity norm of the residuals, $\rho_{Linf,H}$, was also tracked for each solution, where

$$\rho_{Linf,H} = \max_{1 \le i \le N_{v,H}} (|\rho_i|). \quad (11)$$

The following subsections describe the code and solution verification techniques that were used to assess the code accuracy and estimate numerical uncertainty in the computational approach used for this study.

4.1 CODE VERIFICATION

As mentioned previously, the computational solution to the problem is expected to converge to some asymptotic solution as the mesh on the domain is refined. The rate at which the solution converges is referred to as the order of accuracy, p. The formal order of accuracy, p_f, describes the theoretical rate at which the solution is expected to converge, based on the computational method used. In this case, the FE method employed has $p_f=2.0$, meaning that the error in the solution is expected to decrease twice as fast as the decrease in h_H. In order to vet the accuracy of the implemented code (i.e., how accurately the code solves the governing PDE) some reference solution is required.

Often in engineering computation, an exact, analytical solution is sought for a given problem in order to verify that the computational tool properly solves the problem of interest. With respect to governing PDE solutions for complex physics, such as with the heat equation in a porous unit cell, no analytical solution exists. However, the Method of Manufactured Solutions (MMS) circumvents the issue arising from a lack of analytical solution [20]. MMS allows for the user to prescribe an analytical solution—one that does not necessarily reflect real physical behavior. For the method, the MMS form of the governing equation can be presented as

$$k\left(\frac{\partial^2 T_{MMS}}{\partial x^2} + \frac{\partial^2 T_{MMS}}{\partial y^2}\right) + S_{MMS} = 0, \quad (12)$$

where T_{MMS} is the user-prescribed manufactured solution, and S_{MMS} is the heat source distribution associated with the MMS problem. In most cases, trigonometric and/or exponential functions are used to define T_{MMS} because of their conveniently smooth and infinitely differentiable characteristics. With T_{MMS} known (i.e., defined by the user), rearrangement of Equation (12) yields the energy source distribution—as shown in Equation (13)—required across the domain to result in the T_{MMS} temperature distribution.

$$S_{MMS}(x,y) = -k\left(\frac{\partial^2 T_{MMS}}{\partial x^2} + \frac{\partial^2 T_{MMS}}{\partial y^2}\right) \quad (13)$$

For the MMS code verification aspect of a study, the same computational domain as the original problem of interest is used, however, all boundary conditions are modified to respect the manufactured solution. For example, Dirichlet boundary conditions would be set to T_{MMS} along the boundary, and heat flux boundary conditions would be derived based on the spatial derivative of T_{MMS}. For the problem at hand, the manufactured solution used was defined as

$$T_{MMS}(x,y) = \cos(2\pi x)\sin(\pi y + 0.75), \quad (14)$$

and the resulting manufactured heat source distribution is

$$S_{MMS}(x,y) = 5\pi^2 \cos(2\pi x)\sin(\pi y + 0.75). \quad (15)$$

S_{MMS}, is applied across the domain, replacing all source terms associated with the original problem of interest. The temperature boundary conditions for the system of interest, T_Γ, include T_H and T_C, such that

$$T_\Gamma = T_{MMS}. \quad (16)$$

In the original problem of interest, the normal heat flux, q_n, at the adiabatic boundaries is equal to 0.0. With the boundary normal vector, $\boldsymbol{n}$, pointing out of the domain, applied boundary q_n'' for the MMS problem is given to be

$$q_n'' = -\boldsymbol{n} \cdot \begin{Bmatrix} 2\pi k \sin(2\pi x)\sin(\pi y + 0.75) \\ -\pi \cos(2\pi x)\cos(\pi y + 0.75) \end{Bmatrix}, \quad (17)$$

where a positive q_n'' value is heat entering the domain. The governing PDE is then solved computationally using the FE method with the MMS source terms and boundary conditions enforced.

Error can be computed between the computationally-determined temperature solution and the prescribed MMS solution. For this study, both the RMS and L-infinity norm errors, $\varepsilon_{RMS,H}$ and $\varepsilon_{Linf,H}$, respectively, were computed across each mesh H. The error metrics are given in Equation (18) and Equation (19).

$$\epsilon_{RMS,H} = \sqrt{\frac{1}{N_{v,H}} \sum_{i=1}^{N_{v,H}} \left(T_i - T_{MMS,i}\right)^2} \quad (18)$$

$$\epsilon_{Linf,H} = \max_{1 \le i \le N_{v,H}} \left(\left|T_i - T_{MMS,i}\right|\right) \quad (19)$$

The observed order of accuracy is the actual convergence rate of the solution—as opposed to the theoretical convergence rate—determined using the change in error with mesh refinement. In this study, the observed orders of accuracy on mesh H using $\varepsilon_{RMS,H}$ and $\varepsilon_{Linf,H}$ are denoted by $p_{RMS,H}$ and $p_{Linf,H}$, respectively, and are shown in Equation (20) and Equation (21).

$$p_{RMS,H} = \frac{\ln\left(\epsilon_{LRMS,H}/\epsilon_{LRMS,H+1}\right)}{\ln\left(h_H/h_{H+1}\right)} \quad (20)$$

$$p_{Linf,H} = \frac{\ln\left(\epsilon_{Linf,H}/\epsilon_{Linf,H+1}\right)}{\ln\left(h_H/h_{H+1}\right)} \quad (21)$$

It is expected that the observed order of accuracy would converge to p_f with mesh refinement. If the mesh is not refined enough, the solution convergence behavior may be very different from the theoretical behavior. This sometimes erratic or non-theoretical behavior regime is considered the "non-asymptotic egime," whereas the "asymptotic regime" refers to the sufficiently refined mesh solution behavior regime where the solution converges to the asymptotic solution in a near theoretical manner. With these characteristics in mind, the MMS code verification approach provides a convenient tool for debugging code providing credibility evidence towards the correct implementation of the numerical methods used to obtain information on the problem of interest. The notion of asymptotic convergence is used in the solution verification approach in the next subsection to help estimate numerical uncertainty.

4.2 SOLUTION VERIFICATION

Beyond code verification, solution verification is used to estimate the numerical uncertainty in the solution due to discretization. For this study, the global deviation grid convergence index (GCI) was used to estimate U_{num} on k^*. As with MMS in code verification, a series of systematically refined meshes is used to observe the relative SRQ convergence and observed order of accuracy with respect to p_f. As opposed to MMS for code verification, solution verification uses the original problem of interest, with all the original boundary conditions and source terms (if any). For this study, U_{num} was computed only on the finest mesh of each five-mesh refinement series. In this process, the mesh size and k^* values for $H=3$, 2, and 1 were required. An original description of the global deviation GCI process is presented in [21], and other applications of the method for problems similar to those presented in this work can be found in [13-17].

Initially, the modified transcendental order of accuracy, p_t, is computed on the fine mesh as

$$p_t = \ln\left[\left(r_{1,2}^{p_t} - 1\right)\left(\left|\frac{k_3^* - k_2^*}{k_2^* - k_1^*}\right|\right) + r_{1,2}^{p_t}\right] / \ln\left(r_{1,2} r_{2,3}\right), \quad (22)$$

and the global observed order of accuracy deviation, Δp, is subsequently determined from

$$\Delta p = \min\left(\left|p_f - p_t\right|, 0.95 p_f\right). \quad (23)$$

The global deviation factor in Equation (23) expresses by how much the convergence of the solution on the fine mesh appears to deviate from the formally expected behavior, thus the global observed order of accuracy is determined simply as

$$p^* = p_f - \Delta p. \quad (24)$$

A factor of safety term, FS, is scaled between 1.1 and 3.0 based on the relative observed order of accuracy of the SRQ convergence with respect to the formal order of accuracy such that

$$FS = 3.0 - 1.9\left(p^*/p_f\right)^8. \quad (25)$$

From using the FS and the relative convergence behavior of the SRQ on the finest two meshes, numerical uncertainty due to discretization on the fine mesh k^* is estimated as

$$U_{num} = FS\left|\left(k_2^* - k_1^*\right)/\left(r_{1,2}^{p^*} - 1\right)\right|. \quad (26)$$

Equation (26) represents the 95% confidence level uncertainty estimate of the SRQ on the fine mesh. The derivation suggests that the uncertainty estimate is scaled based on proximity of the SRQ convergence behavior to the asymptotic regime. Thus, the closer the solution appears to be to asymptotic regime, the smaller the uncertainty estimate. Note that this method considers

observed convergence rates better than the theoretical rate to be penalized the same as observed converge rates worse than theoretical, hence the title of global "deviation."

The following section describes results for the system of interest, including MMS code and GCI solution verification.

5. RESULTS AND DISCUSSION

The following subsections address the MMS code verification results and the system behavior of the problem of interest, including numerical uncertainty estimate results.

5.1 CODE VERIFICATION: MMS

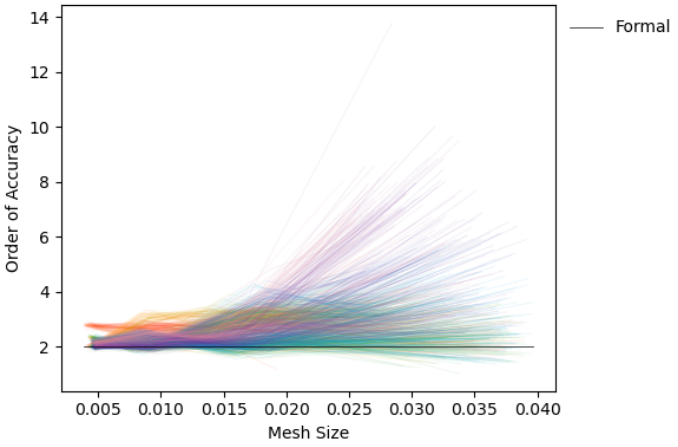

Figure 6. MMS observed order of accuracy using RMS error converges approximately to formal order of accuracy with mesh refinement

Using the MMS approach for each porosity level modeled between 1% and 78% and each polygon representation with N_{sides} between 3 and 100, 1176 MMS studies were performed. Figure 6 and Figure 7 show the RMS and L-infinity norm MMS solution observed order of accuracy convergence behaviors with mesh refinement for each of the five-mesh domain mesh series. Note than for both error computation approaches and for all mesh series, the observed order of accuracy approximately approaches the formal second-order accurate behavior. This trend lends credibility evidence for the subsequent results presented for the problem of interest, where the convergence of the solution on the fine mesh is near the theoretical convergence rate and is consistently so across all 1176 mesh series, suggesting correct implementation of the numerical method.

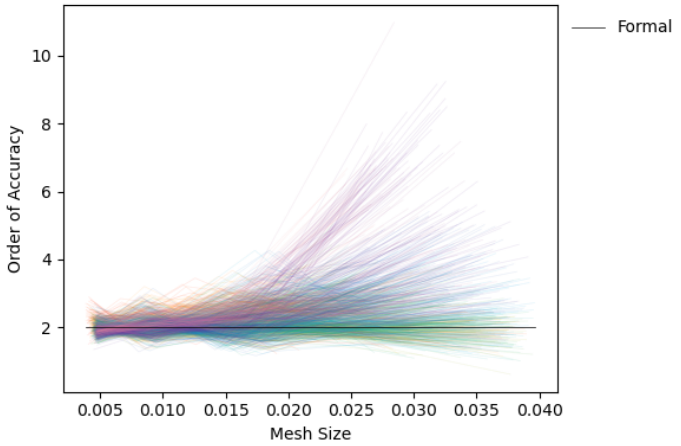

Figure 7. MMS observed order of accuracy using L-infinity norm error converges approximately to formal order of accuracy with mesh refinement

5.2 PROBLEM OF INTEREST

On the problem interest, each circular pore was represented by a series of polygonal pores with N_{sides} ranging from 3 to 100. As the number of sides increases, the true model porosity asymptotically approaches the underlying circular pore system porosity. For each of the underlying circular porous systems, Figure 8 shows the convergence of the actual model porosity to the underlying system porosity. Likewise, Figure 9 shows the relative change in model porosity from N_{sides} to $N_{sides}+1$ normalized by the underlying circular pore porosity. Note in both figures that the model porosity appears to be qualitatively converged using between 20 and 40 polygon sides. Note that in Figure 9 all of the system curves are identical as the normalized model porosity is not dependent on absolute porosity but only relative geometry.

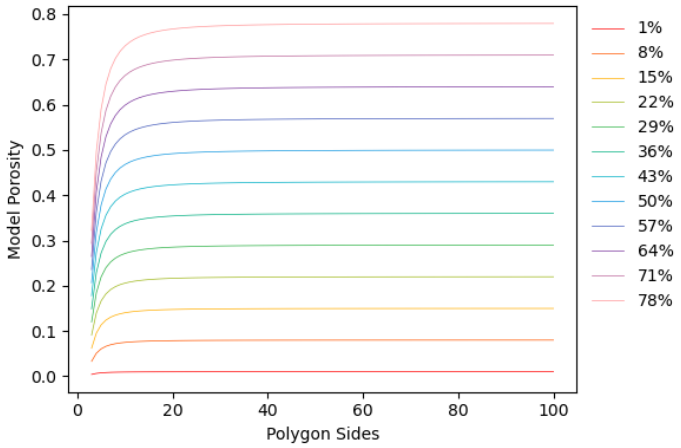

Figure 8. Polygonal model porosity converges asymptotically to circular system porosity

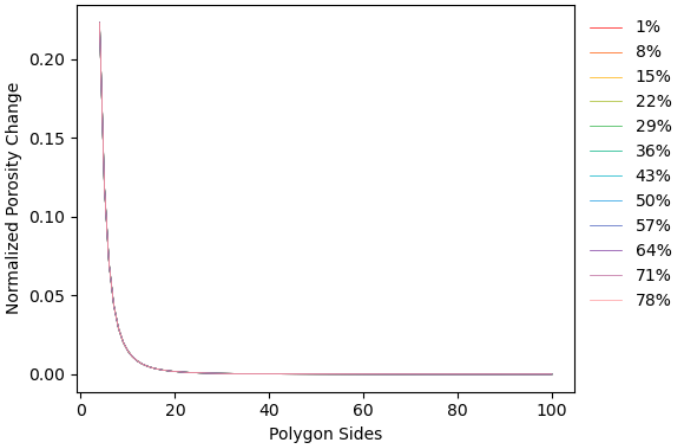

Figure 9. Rate of change of polygonal model porosity normalized by circular porosity with increasing number of polygonal pore sides

Figure 10 illustrates the qualitative convergence of the temperature distribution on the problem of interest for a series of five systematically refined meshes, where Figure 10a through Figure 10e are solutions on mesh *H=5* through *H=1*, respectively. Note the apparent qualitative convergence with mesh refinement, especially by mesh *H=1*.

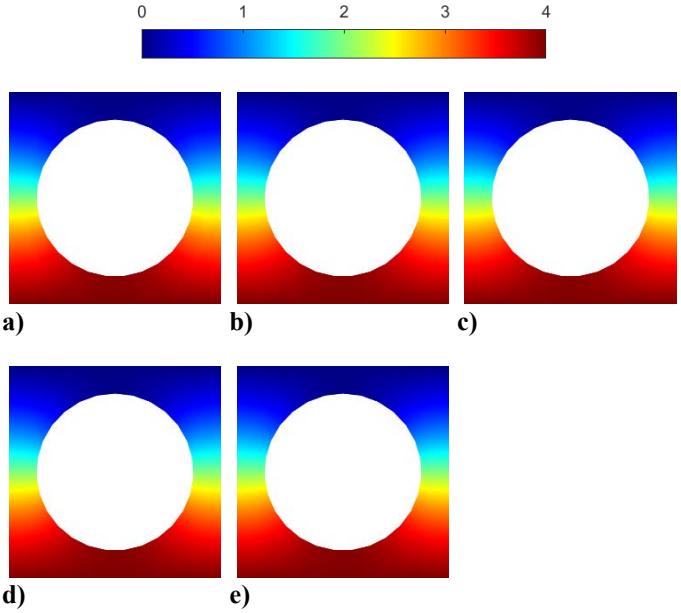

Figure 10. Computational temperature contours qualitatively converge with mesh refinement

Figure 11 shows an example of the fine mesh temperature contours for a single underlying circular porosity for six of the first 23 polygonal pore representations indicated by N_{sides} 3, 5, 8, 12, 17, and 23. The porosity of a polygonal model pore with 23 sides is 99.76% of the underlying circular pore porosity. Note that with an increase in N_{sides}, the model pore converges towards a circular shape, and the temperature contour in the domain converges in a like manner. It is critical to note the obvious asymmetry of the temperature contours in the *y* direction for the pores with an odd number of sides. Likewise, the geometric effects of the pore geometry on the qualitive temperature distribution shape are readily apparent on systems with lower number of pore sides.

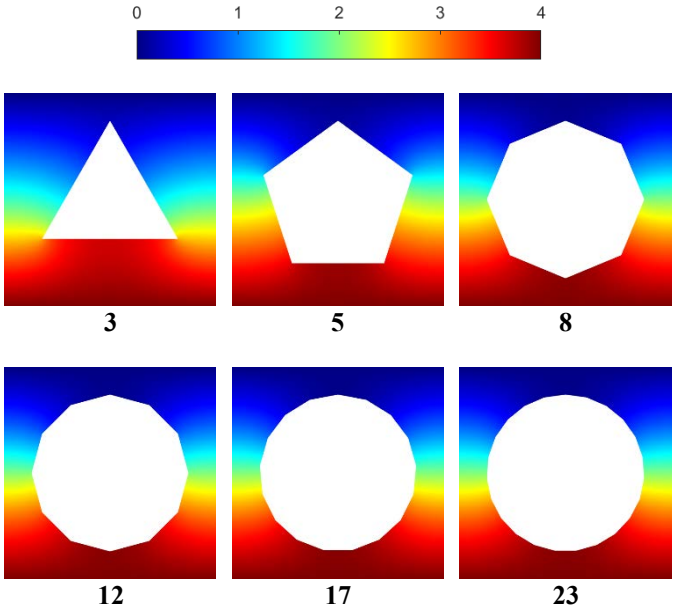

Figure 11. Computational temperature contours qualitatively converge with increasing polygon sides

Figure 12 presents the actual effective thermal behavior of the porous systems with respect to N_{sides} and coordinated by porosity. The black error bars in the plot indicate the U_{num} values as determined by the GCI approach, again representing the 95% confidence level. In most cases, the U_{num} is extremely low with the median uncertainty estimate at 0.022% of the fine mesh k^* value. The minimum and maximum U_{num} values were 0.0003% and 30.5% of the fine mesh k^* values, where only 7 of the 1176 fine mesh data points had numerical uncertainty estimates greater than 10.0%. Of those 1176 data points, 1105 had uncertainty estimates below 1.0% of the fine mesh k^* values. Note in Figure 13 that as the porosity level increases, the fine mesh k^* value begins to oscillate with lower N_{sides}. Such oscillatory behavior is expected due to the increasingly significant effects of pore geometry with increased porosity. The behavior is studied in part in [14] and is not surprising. Despite and low-N_{sides} behavior, each porosity system eventually converges towards some circular k^* response. Some of the larger uncertainty estimates could be due to meshing limitations in the mesh generator, low quality mesh regions with the extreme low and high porosity systems, and early converged solutions on lower porosity domains. In Figure 13, the markers indicate the solution point at which increasing the number of polygon sides begins changing the resultant k^* value by less than 1% of the

$N_{sides}=100$ k^* value, approximating a roughly 99% converged response with respect to geometric representation. The discrepancy between the low N_{sides} models and the converged $N_{sides}=100$ responses illustrates model form error, as opposed to the numerical error estimated using solution verification. Thus, these results have approximately segregated the two error sources for these analyses.

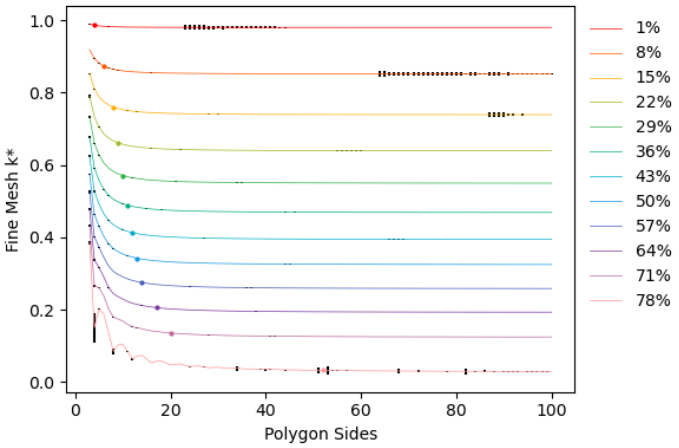

Figure 12. k^* values converge in apparent asymptotic behavior with relatively low numerical uncertainty

The results presented here show that geometric representation of a porous system void can play a significant role in the effective thermal response of the domain. Whereas the system requires a polygon with roughly 20 to 40 sides to effectively represent the porosity of the system, most all of the systems required well below 20 sides to effectively capture the effective thermal conductivity of the systems. It is evident, however, that with increasing porosity, the risk of introducing model form error into the solution also increases, thus geometric fidelity can have a significant impact on the level of error present in the computed effective thermal response of the porous system.

6. CONCLUSION

This paper has presented a thorough analysis of the effective thermal response of a two-dimensional porous system using the finite element method, where polygons were used to represent circular pores in computational models. Code verification was performed using the Method of Manufactured solutions to show an approximately second-order accurate FE implementation, and solution verification was used to estimate numerical uncertainty in k^* of the porous system due to discretization. Numerical uncertainties were shown to be relatively low with very few exceptions. In this work, model form error was illustrated due to geometric fidelity, where polygonal representation of a circular pore impacted the effective thermal response of the system. The computational trends show that systems with larger porosities require a higher number of polygon sides to effectively capture the circular pore's effective thermal response.

REFERENCES

[1] Ibrahim, T. K. and Rahman, M. M., 2013, "Study on effective parameter of the triple-pressure reheat combined cycle performance," Thermal Science, 17(2), pp. 497-508.

[2] Fathi, N., McDaniel, P., Forsberg, C., and de Oliveira, C., 2018, "Power Cycle Assessment of Nuclear Systems, Providing Energy Storage for Low Carbon Grids," Journal of Nuclear Engineering and Radiation Science, 4(2), 020911.

[3] Hunter, I., Daleo, J., Wilson, J., and Ellison, K., 1999, "Analysis of Hot Section Failures on Gas Turbines in Process Plant Service," Proceedings of the 28th Turbomachinery Symposium, 28, pp. 9-20.

[4] Slaehnasab, B., Poursaeidi, E., Mortazavi, S. A., and Farokhian, G. H, 2016, "Hot corrosion failure in the first stage nozzle of a gas turbine engine," Engineering Failure Analysis, 60, pp. 316-325.

[5] Fathi, Nima, Patrick McDaniel, Seyed Sobhan Aleyasin, Matthew Robinson, Peter Vorobieff, Sal Rodriguez, and Cassiano de Oliveira. "Efficiency enhancement of solar chimney power plant by use of waste heat from nuclear power plant." Journal of Cleaner Production 180 (2018): 407-416.

[6] Gobetz, Z., Rowen, A. Dickman, C., Meinert, K., and Martukanitz, R., 2016, "Utilization of Additive Manufacturing for Aerospace Exchangers," Office of Naval Research, Final Report.

[7] Zhang, S., Lane, B., Whiting, J., and Chou, K., 2018, "An Investigation into Metallic Powder Thermal Conductivity in Laser Powder Bed Fusion Additive Manufacturing," Proceedings of the 19th Annual International Solid Freeform Fabrication Symposium – An Additive Manufacturing Conference, pp. 1796-1807.

[8] Ibrahim, Y., Elkholy, A., Schofield, J. S., Melenka, G. W., and Kempers, R., 2020, "Effective Thermal Conductivity of 3D-printed Continuous Fiber Polymer Composites," Advance Manufacturing: Polymer & Composites Science, 6(1), pp. 17-28.

[9] Danes, F., Garnier, B., and Dupuis, T., 2003, "Predicting, Measuring, and Tailoring the Transverse Thermal Conductivity of Composites from Polymer Matrix and Metal Filler," International Journal of Thermophysics, 24(3), pp. 727-734.

[10] Zhao, J.-J., Duan, Y-Y., Wang X.-D., 2012, "Experimental and analytical analyses of the thermal conductivities and high-temperature characteristics of silica aerogels based on microstructures," Journal of Physics D: Applied Physics, 46, 015304.

[11] Irick, K. W., 2017, "Effective Thermal Resistance Comparison of Aerogel and Multi-Layer Insulation as Radiative Barriers Using the Single-Sided Guarded Hot Plate Method," Frontiers in Heat and Mass Transfer, 8(2).

[12] Wu, S., Li, T., Tong, Z., Chao, J., Zhai, T., Xu, J., Yan, T., Wu, M., Xu, Z., Bao, H., Deng, T., and Wang, R., 2019, “High-Performance Thermally Conductive Phase Change Composites by Large-Size Oriented Graphite Sheets for Scalable Thermal Energy Harvesting.” Advanced Materials, 31(49), 1905099.
[13] Irick, Kevin, and Nima Fathi. "Computional Evaluation of Thermal Response of Open-Cell Foam with Circular Pore." Journal of Verification, Validation and Uncertainty Quantification (2020).
[14] Irick, Kevin, and Nima Fathi. "Evaluation of Pore Geometry Effects on Porous Cell Thermal Behavior." In Verification and Validation, vol. 83594, p. V001T08A002. American Society of Mechanical Engineers, 2020.
[15] Irick, Kevin, and Nima Fathi. "High-Fidelity Calculation of Effective Thermal Response of Composite Media With Heat Generation Source." In Verification and Validation, vol. 83594, p. V001T08A003. American Society of Mechanical Engineers, 2020.
[16] Irick, Kevin, and Nima Fathi. "Computational Evaluation of Thermal Barrier Coatings: Two-Phase Thermal Transport Analysis." In Verification and Validation, vol. 41174, p. V001T12A002. American Society of Mechanical Engineers, 2019.
[17] Irick, Kevin, and Nima Fathi. "Thermal Response of Open-Cell Porous Materials: A Numerical Study and Model Assessment." In Verification and Validation, vol. 40795, p. V001T03A002. American Society of Mechanical Engineers, 2018.
[18] Geuzaine, C. and Remacle, J.-F., 2009, “Gmsh: a three-dimensional finite element mesh generator with built-in pre- and post-processing facilities,” International Journal for Numerical Methods in Engineering 79(11), pp. 1309-1331.
[19] Kevin, Irick. “Numerical Evaluation of Effective Thermal Response of Heterogeneous Materials.” (2020).
[20] Roache, P. J., 2009, Fundamentals of Verification and Validation, Hermosa Publishers, Socorro, NM.
[21] Phillips, T. S. and Roy, C. J., 2016 “A New Extrapolation-Based Uncertainty Estimator for Computational Fluid Dynamics,” Journal of Verification, Validation and Uncertainty Quantification, 1(4), pp. 041006-1, 041006-13.